Nano Energy 63 (2019) 103820

Contents lists available at ScienceDirect

Nano Energy

journal homepage: www.elsevier.com/locate/nanoen

Full paper

Capturing the differences between lithiation and sodiation of nanostructured TiS_2 electrodes

Pu Hu[a], Bo Wang[a], Dongdong Xiao[b], Katerina Aifantis[a,*]

[a] Department of Mechanical and Aerospace Engineering, University of Florida, Gainesville, 32603, USA
[b] Department of Mechanical Engineering & Materials Science and Engineering Program, State University of New York at Binghamton, Binghamton, NY, 13902, USA

ARTICLE INFO

Keywords:
Na-ion battery
TiS_2
Stability
Fracture
Cathodes

ABSTRACT

In this study TiS_2 is chosen as a model electrode material to investigate the relationship between the electrochemical and mechanical performance of layered cathodes for Na-ion batteries. Employing $NaFP_6$ in EC/DMC as the electrolyte allowed for the most promising electrochemical properties recorded in the literature, namely a reversible capacity of 203 mAh g^{-1} at 0.2 C and 88 mAh g^{-1} at 10 C with a capacity retention of 92% over 50 cycles. Despite this promising performance the capacity still decayed during long term cycling. In-situ x-ray diffraction and high-resolution transmission electron microscopy imaging revealed that TiS_2 underwent a large expansion of 17.7% along the *c* direction and irreversible phase transformations took place during the sodiation/de-sodiation process, which lead to severe mechanical strains and intragranular cracks. In comparison, the mechanical stability of TiS_2 in Li-ion cells was significantly higher. The experimental results are interpreted within a continuum mechanics model which revealed that the maximum effective von Mises stress that is present at the interface between the ion-intercalated TiS_2 and pristine TiS_2 is about four times higher during sodiation than lithiation indicating that the electrode is more susceptible to failure/fracture during sodiation.

1. Introduction

Sodium-ion batteries (SIBs) have been receiving increased attention as alternatives to Li-ion batteries in grid storage systems due to the abundance and lower cost of Na. Despite the great progress in developing new electrode materials with a high capacity, they lack long term electrochemical stability and therefore the practical application of SIBs remains a challenge [1–5]. Na-ion and Li-ion batteries display many similarities, the most common being that Li compounds that are promising cathodes for Li-ion cells can be used in Na-ion batteries by replacing the Li with the Na. Therefore many layer-structured oxides derived from Li compounds have been explored as cathodes for SIBs (such as Na_xCoO_2, $NaNi_{1/3}Fe_{1/3}Mn_{1/3}$, $Na_xFe_{1/2}Mn_{1/2}O_2$) [6–9]. LIBs and SIBs undergo similar intercalation reactions at the cathode and anode, but Na-ion batteries are prone to worse cycle stability due to the larger Na^+ ionic radius (1.02 Å) when compared with Li^+ (0.76 Å) [1,10]. This leads to complicated phase transformations and larger volume changes during sodiation/de-sodiation. The most promising cathode material, reported thus far, is P2-type layered $Na_{1-x}MO_2$ (M = Fe, Mn, Co) which allows for an initial capacity of 190 $mAhg^{-1}$ that can be retained for 150 $mAhg^{-1}$ over 30 cycles [6]. Compared to oxides, layered transition-metal dichalcogenides provide a more flexible structure and higher conductivity due to the weaker van der Waals forces, making such materials also attractive as cathodes [11–16]. TiS_2, the typical S-Ti-S layer consisting of two hexagonal sheets of S and a sheet of Ti, has garnered attention as a potential host material for intercalating Li^+, Na^+, K^+ and Mg^{2+} [17–20]. The reversible capacity and voltage profile of TiS_2 for each electrochemical system is related to the ionic radius of the ion species. First-principle calculations have revealed that Li^+ preferred to occupy the octahedral site between Ti-S_6, thus rendering a flat voltage plateau with a solid-solution evolution during lithation/delithiation. In contrast to Li^+, Na^+ due to its larger ionic radius occupies two different sites (octahedral and tetrahedral site) associated with the concentration of Na in layered Ti-S_6, leading to the formation of multiple phases and consequently multiple voltage plateaus [21,22]. Therefore, Na/TiS_2 and Li/TiS_2 batteries exhibit different electrochemical properties.

Another factor that determines the stability of SIBs is the electrolyte [23]. The electrolyte plays a significant role on the electrochemical performance particularly when the intercalation species have a large ionic radius such as Na^+ and K^+. This is because the intercalation process is sensitive to the properties of the electrolyte in terms of the molecular size, the functional groups and the polarities of electrolytic salt and solvents. For instance, graphite is known to be an anode

* Corresponding author.
E-mail address: kaifantis@ufl.edu (K. Aifantis).

https://doi.org/10.1016/j.nanoen.2019.06.016
Received 25 March 2019; Received in revised form 1 May 2019; Accepted 8 June 2019
Available online 12 June 2019

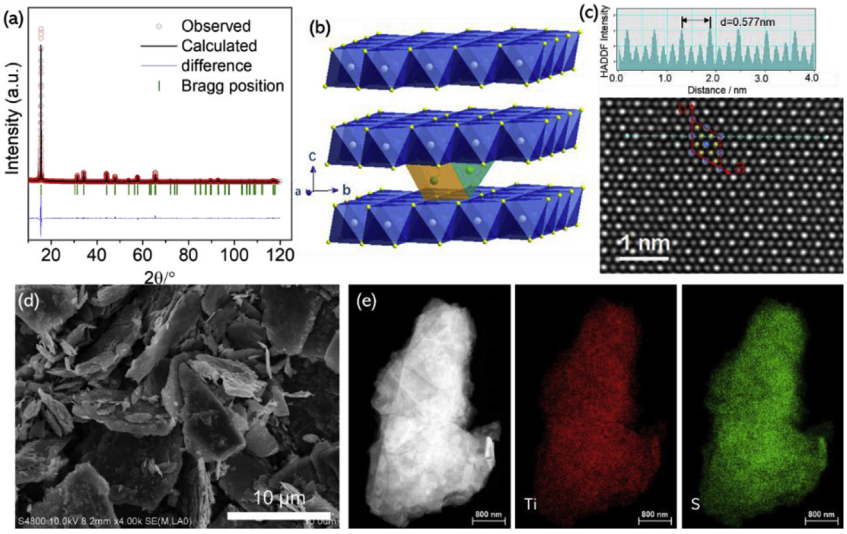

Fig. 1. (a) XRD pattern of TiS_2 nanoparticles. (b) Crystal structure of TiS_2 with Na^+ occupied in octahedral and tetrahedral site. (c) STEM-HAADF image of TiS_2 along the [001] projection and intensity profiles along the indicated line. (d) SEM image of TiS_2 particle, (e) STEM image and the corresponding Ti, S element map for TiS_2 particle.

material for commercial Li-ion batteries, but is considered inactive for Na^+ intercalation in a traditional carbonate-based electrolyte, while it exhibits a reversible capacity of 110 $mAhg^{-1}$ as well as good capacity retention in glyme electrolyte (ether-based electrolyte) [24–26]. Similarly, layered TiS_2 exhibited improved electrochemical properties when it was cycled against K^+ in an ether-based electrolyte instead of a carbonate-based electrolyte [27]. However, cycling Na/TiS_2 in an ether-based electrolyte showed poor cycling stability as the initial reversible capacity of 210 $mAhg^{-1}$, rapidly decayed to 120 mAh/g after 40 cycles [28]. Cycling TiS_2 in a carbonate electrolyte gave a lower initial reversible capacity (~146 mAh/g at 0.1C), which however had a good retention after 50 cycles at a low current rate [29].

In this work, layered TiS_2 was chosen as a model electrode material to investigate electrochemically-induced mechanical degradation in SIBs. Various electrolyte solutions were used to obtain the most stable electrochemical performance and subsequently in-situ x-ray diffraction (XRD) and high-resolution transmission electron microscopy (HR-TEM) were performed to capture the evolution of phase transformations and structural stability during the sodiation and de-sodiation process. To interpret the experimental observations continuum mechanics modelling was employed to illustrate the difference between the lithiation- and sodiation-induced stresses that TiS_2 electrodes undergo. To the best of our knowledge, this is the first report on the structural and mechanical degradation for layered cathodes in Na-ion batteries. Our insight will further help in the quest to make SIBs viable.

2. Experimental section

2.1. Electrochemical measurements

TiS_2 powder (200 mesh; 74 μm) was purchased from Sigma-Aldrich. Porous electrodes were fabricated using a mixture of TiS_2 as the active material, carbon black and binder in the weight ratio of 8:1:1. The TiS_2, acetylene black and sodium carboxyl methyl cellulose (CMC) were mixed with DI-H_2O to obtain a homogenous slurry, which was then cast onto Al foil current collectors, and dried at 60 °C under vacuum for 24 h. The active material loading per electrode was ~3 mg cm^{-2}. CR2032 coin-cells were assembled in an argon-filled glovebox. For the Na battery, Na metal and glass fiber were used as the counter electrode and separator, respectively. To stabilize the interaction between the electrode and the electrolyte, three electrolyte solutions were considered as follows: (i) 1 M $NaPF_6$ dissolved in ethylene carbonate/diethyl carbonate (EC/DMC) with a volume ratio of 1:1; (ii) 1 M $NaClO_4$ dissolved in EC/DMC; (iii) 1 M sodium trifluoromethanesulfonimide (NaTFSI) dissolved in tetra ethylene glycol dimethyl ether (TEGDME) and (iv) 1 M $NaPF_6$ dissolved in diethylene glycol dimethyl ether (DGME). 5% fluoroethylene carbonate (FEC) was added into the EC/DMC electrolytes as an additive to stabilize the Na metal anode.

For comparison purposes Li cells were also assembled using the same TiS_2 electrodes but with pure Li metal and glass fiber as the counter electrode and separator, respectively. 1 M $LiPF_6$ dissolved in EC/DMC (volume ratio of 1:1) with 5% FEC additive was used as the electrolyte.

Both Na-ion and Li-ion cells were cycled under a constant current charging/discharging mode in the potential range of 1.0–3.0 V at a varied C-rate using an Arbin 2000 battery tester. Galvanostatic intermittent titration technique (GITT) was performed by charging/discharging at 0.2 C for 1 h and relaxing for 1 h to the equilibrium state and then repeating this process for the full voltage window of operation. Electrochemical impedance spectroscopy (EIS) was performed in the frequency range of 100 kHz to 100 mHz with an excitation amplitude of 5 mV.

2.2. Materials characterization

The crystal structure of the pristine TiS_2 powder and cycled electrodes was characterized by x-ray diffraction (X'Pert Powder) (XRD) with a step size of 0.01° (2θ) in the range of 5–120°. The morphology before and after cycling was examined using a FEI Tecnai F20 high resolution transmission and scanning electron microscope (HRTEM/STEM) that operated at 200 kV and was equipped with electron diffraction spectroscopy (EDS) and selected area electron diffraction (SAED). To characterize the cycled cathodes, the cells were opened in an Ar-filled glove-box, and the electrodes were washed with dimethyl carbonate to remove electrolyte salt, and then powder was scrapped onto the TEM grid. The HR-TEM images were used to obtain the strain fields and corresponding strain components using the geometric phase analysis (GPA) method [30] by the strain Digital Micrograph plug-in program.

3. Results and discussion

3.1. Structural and chemical compositions

Fig. 1a depicts the XRD pattern of pristine TiS_2, of which all the diffraction peaks could be indexed to be P-3m1 (No. 164) space group of TiS_2 and no impurity peaks were found. The calculated cell parameters were a = b = 3.407 Å and c = 5.698 Å, agreeing with the literature values [17,29]. The strongest peak at 2θ = 15.5° belongs to the diffraction of the (001) lattice plane, indicating a highly preferred

orientation along the (001) direction. A simulated crystal structure shown in Fig. 1b depicts the layered structure along the [100] direction, which consists of two-dimensional layers of edge-linked octahedral TiS_6. The gap between the layers, which are connected by van der Waals forces provides a network of vacant octahedral and tetrahedral sites, permitting the intercalation of guest species, such as Li^+, Na^+, K^+ and Mg^{2+}. The layer distance calculated by refinement (5.698 Å) is larger than the ionic radius of Na^+, thus allowing for intercalation.

A high-angle annular dark field (HAADF) STEM image of TiS_2 along the [001] projection is shown in Fig. 1c, in which the sulfur and titanium columns can be clearly observed; bright spots correspond to Ti columns, while darker spots correspond to S columns. Orderly arrangement of S and Ti atoms confirms the crystalline structure of TiS_2. The distance between Ti columns from the intensity profiles along the indicated line is 0.577 nm, and the calculated cell parameters are a = b = 0.33 nm, which is consistent with the XRD results. Both XRD and STEM results revealed that the TiS_2 had a high crystallinity and a highly ordered atomic arrangement. Fig. 1d depicts an SEM image presenting the typical morphology of a TiS_2 particle that is micro-sized with an irregular morphology. Energy dispersive spectroscopy (EDS) mapping showed that both S and Ti were homogenously distributed (Fig. 1e). Moreover, the semi-quantitative analysis of the S/Ti mole ratio was estimated to be 1.9, which is close to the value of the ideal stoichiometric ratio of TiS_2.

3.2. Electrochemical performance

Fig. 2 compares the capacity retention and voltage profiles when the cells were cycled using different electrolytes. Fig. 2a shows that the Na/TiS_2 batteries using ether-based electrolytes (1 M NaTFSI-TEGDME and 1 M $NaPF_6$-DGME) exhibited similar cycling behavior, since the capacity decayed rapidly from 201 mAh g^{-1} to 136 mAh g^{-1} after 50 cycles, corresponding to a capacity retention of 67.5%. The batteries using carbonate-based electrolytes (1 M $NaPF_6$-EC/DMC, 1 M $NaClO_4$-EC/DMC) displayed a stable specific capacity of 185 $mAhg^{-1}$ with a superior capacity retention of 92% after 50 cycles at 0.5 C. This reversible capacity is higher than that recently reported of 146 $mAhg^{-1}$ at 0.1 C in carbonate-based electrolytes [29]. It has been revealed that the electrochemical performance of sulfides significantly depends on the composition of the electrolyte and the nanostructure of the electrode material. A recent report [31] showed that ultrathin TiS_2 nanosheet cathodes in SIBs displayed a higher specific capacity in a TEGDME electrolyte than in a carbonate electrolyte, however, the capacity was unstable since it increased with each cycle. Another study [32] found that the van der Waals forces between the layered structure of bulk TiS_2 electrodes could be reduced by the co-intercalation of organic solvents (DGME, DMSO), resulting into the exfoliation of the TiS_2 layers.

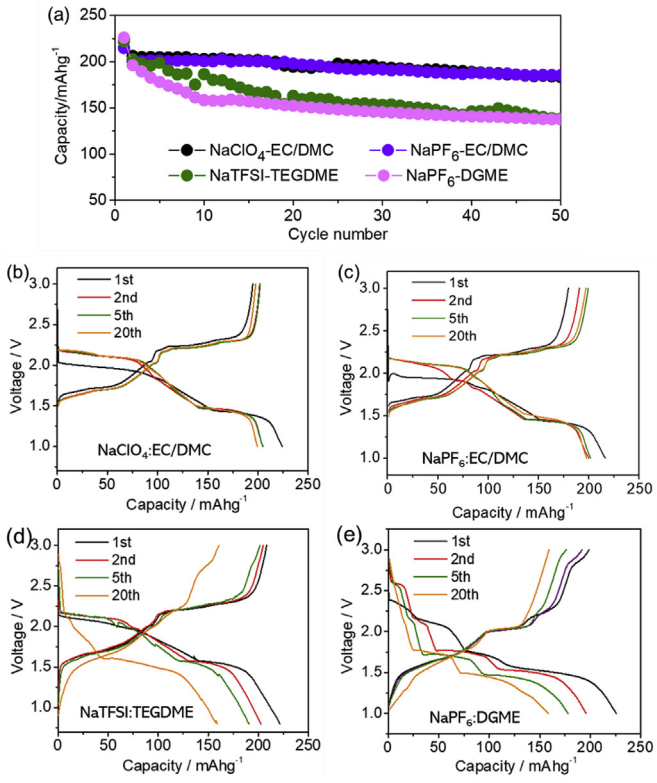

Fig. 2. (a) Comparison of the cycling stability of TiS_2 electrodes in different electrolytes. Galvanostatic discharge-charge curves of TiS_2 using $NaClO_4$: (b) EC/DMC, (c) $NaPF_6$: EC/DMC, (d) NaTFSI:TEGDME, (e) $NaPF_6$:DGME (e) as electrolyte.

XRD (Fig. S1) revealed that in DGME electrolyte, a new diffraction peak appeared at 7.8°, during the initial sodiation, demonstrating that the interplanar distance of the material expanded to 1.14 nm. Moreover, the (001) peak of TiS_2 remained at the discharged state, implying that TiS_2 is not fully sodiated in ether-based electrolytes. The stability of the electrode at a charged state was compared by monitoring the open circuit voltage (OCV) at 100% state of charge (Fig. S2). The cells were charged to 3.0 V at 0.5 C and held there for 72 h. The cells employing a carbonate-based electrolyte showed a steady open-circuit voltage (OCV) of 2.2 V (Fig. S2a) and delivered a high capacity of 202 $mAhg^{-1}$ (almost 100% of the charge capacity) (Fig. S2b). In contrast, the cells using DGME electrolyte underwent severe self-discharge, since the OCV gradually decayed to 1.85 V and a 50% capacity loss occurred during the holding period (Fig. S2c). This result demonstrates that carbonate-based electrolyte solvents are more compatible than ether-based electrolytes with TiS_2 electrodes during Na^+ intercalation.

In Fig. 2b–d, the charge-discharge curves for the first cycle show multistep potential plateaus that exhibit prominent flat plateaus at the potentials ~2.1 V and ~1.4 V (vs. Na^+/Na), which is consistent with previous reports for Na/TiS_2 cells at room temperature [28,29]. The voltage curves for the battery using $NaPF_6$-DGME as the electrolyte show more plateaus. The phenomenon of multiple voltage plateaus is commonly observed in layered oxide cathodes for SIBs, which implies multi-phase transformation of the electrode material during the charge/discharge process. This is quite distinct from the behavior of Li^+ intercalation. The voltage curves of Li/TiS_2 batteries exhibit a typical S-shaped variation (Fig. S3, supporting information), demonstrating the solid-solution evolution from TiS_2 to Li_xTiS_2 during charge/discharge. Therefore, TiS_2 undergoes more complicate phase changes in Na/TiS_2 cells than in Li/TiS_2 cells, which results in a disparate impact on the battery performance especially on the electrode stability for long-term cycling.

Previous studies of TiS_2 electrodes trace the capacity decay in SIBs to the deterioration of the first plateau (~2.1 V) upon continuous cycling [28]. This phenomenon is consistent with our observations when the ether-based electrolyte was used. As shown in Fig. 2d and 2e, the plateau at ~2.1 V decreased upon cycling and almost disappeared after 20 cycles in TEGDME and DGME-based electrolytes. The batteries with carbonate-based electrolyte exhibited a stable voltage profile during cycling and the potential curves maintained the same shape and two stable flat plateaus at the initial cycle. Therefore, it was demonstrated that the electrolyte played a significant role in promoting or suppressing the deterioration of the higher plateau. Moreover, when cycled with $NaPF_6$-EC/DMC electrolyte, the discharge and charge capacities during the first cycle of the Na/TiS_2 cell were 225 mAh g^{-1} and 205 mAh g^{-1}, corresponding to an intercalation of 0.94 Na^+ per TiS_2 and reversible de-intercalation of 0.85 Na^+. This indicated a high Coulombic efficiency during the electrochemical process.

To investigate the kinetics and thermodynamics behavior of Na^+ intercalation/de-intercalation into TiS_2, GITT was carried out. As

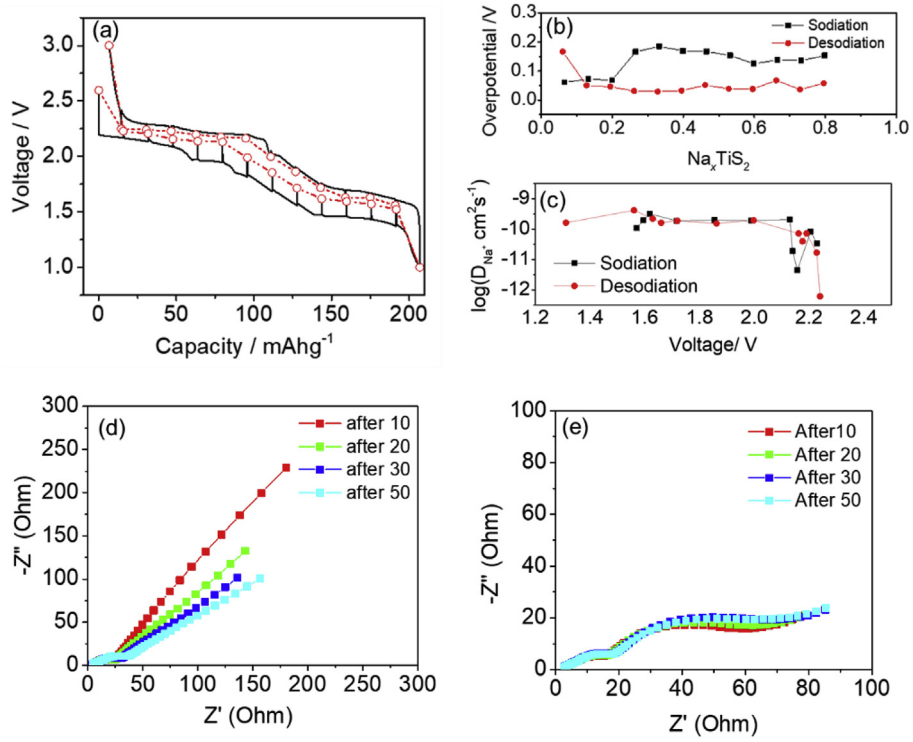

Fig. 3. (a) GITT curves of TiS_2 at the first cycle, (b) Overpotential estimated from the difference between the equilibrium potential and the transient potential from GITT curves, (c) Diffusion coefficient of Na^+ in TiS_2 electrode during sodiation/de-sodiation. Electrochemical impedance spectroscopy of (d) Na/TiS_2 and (e) Li/TiS_2 cell at different cycles.

shown in Fig. 3a, the thermodynamic equilibrium potential (red dashed lines) contains two flat plateaus and a slope. The difference between the equilibrium potential and the transient potential depicts the over-potential for the electrochemical process of Na^+ intercalation/de-intercalation into TiS_2, which results mainly from the Ohm polarizations, sluggish mass diffusion and charge transfer. It can be seen in Fig. 3b that the over-potentials were ~0.18 V during Na^+ intercalation but decreased to ~0.05 V during the following de-intercalation, showing a low overpotential. The diffusion coefficients of Na^+ (D_{Na+}) in the TiS_2 electrode could be estimated from GITT for each step of single titration (Fig. 3c and Fig. S4). The D_{Na+} value was $\sim 1.8 \times 10^{-10}\ cm^2\ s^{-1}$ at a low plateau, which is slightly higher than D_{Na+} ($\sim 3.2 \times 10^{-11}\ cm^2\ s^{-1}$) at a high plateau. The overall D_{Na+} values are in the order of $10^{-10}\ cm^2\ s^{-1}$ for TiS_2. Fast ionic diffusion and weak polarizations bring about the rapid charge transfer of the electrochemical process, thereby promoting the high-rate capability of TiS_2.

EIS spectra of Na/TiS_2 were obtained at an open-circuit voltage after different cycles to reveal the impedance evolution upon cycling. Nyquist plots of the EIS spectra for Na/TiS_2 cells at various cycles are compared in Fig. 3d. Each spectrum contains a depressed semicircle at a high frequency and the following slope line in the low frequency. The semicircle at the high frequency is ascribed to the charge transfer resistance (R_{ct}) between the electrode and electrolyte. It can be found that the intercept of the semicircle with the real part of the impedance (Z') gradually increased with cycling, indicating the continuous increase of charge transfer resistance after the repeated Na^+ intercalation/de-intercalation process. In comparison, Nyquist plots of the EIS spectra for Li/TiS_2 cells (Fig. 3e) are shown to maintain the same shape with different cycles and the semicircles are much smaller than the ones for Na/TiS_2. This demonstrates that the intercalation of Li into TiS_2 cells is more stable with a faster charge transfer process than intercalation of Na^+.

The rate capability of TiS_2 electrodes for SIBs using $NaPF_6$ in EC/DMC as the electrolyte is illustrated in Fig. 4a, which presents that the capacity decreased slowly as the rate increased from 0.5 C to 10 C. A discharge capacity of 185 mAh g^{-1} and 158 mAh g^{-1} was observed at a rate of 0.5 and 1 C, respectively, and decreased slightly with increasing C-rate. At a rate of 5 C, the electrode exhibited a high capacity of 117 mAh g^{-1}, corresponding to 74% of the capacity at 1 C. Even at 10 C, it still had a capacity of 88 mAh g^{-1}, indicating that the electrode material delivered an excellent high-rate capability. This result is much better than previous reports (~100 mAh g^{-1} at 1.7C) [29]. In addition, it can be clearly seen that the separation of the potential between the charge and discharge plateau increased slightly with increasing the C-rate (Fig. S5), showing weak polarization of the electrochemical process between the electrode and electrolyte. Therefore, we believe that the superior rate capability of these SIBs stems from the good interfacial compatibility between the electrode and electrolyte, which allows the fast charge transfer during the electrochemical process.

Although the cycling stability and rate capability of TiS_2 cathodes were improved by optimizing the electrolyte, the capacity still decayed after long-term cycling. Fig. 4b compares the capacity retention of Na/TiS_2 and Li/TiS_2 cells, cycled in similar electrolyte solutions (1 M $NaPF_6$-EC/DMC for Na/TiS_2, 1 M $LiPF_6$-EC/DMC for Li/TiS_2). Na/TiS_2 showed an 80.2% capacity retention over 100 cycles, while Li/TiS_2 batteries exhibited almost no capacity decay, showcasing a much better cycling stability. This means that the electrochemical stability of TiS_2 still needs to be improved to make SIBs viable as energy storage systems for practical applications.

3.3. Mechanical and structural evolution of TiS_2 during sodiation/desodiation

The in-situ XRD results over the first two cycles, shown in Fig. 5a, depict that the intensity and position of the (001) diffraction peak clearly evolves with the state of charge during the first charge/discharge. During the sodiation process, three new phases formed. Multi-phase transformation accompanied with an increase of the *c* parameter occurred during the first plateau, where the pristine TiS_2 (phase 1) transformed entirely to the first new phase (phase 2) at the beginning of sodiation, then phase 2 rapidly disappeared and another new phase (phase 3) formed at the end of the first plateau. The lattice parameter was calculated based on the (001) peak, which expanded 17.7% along the c direction from 5.698 Å to 6.921 Å during this process. Upon

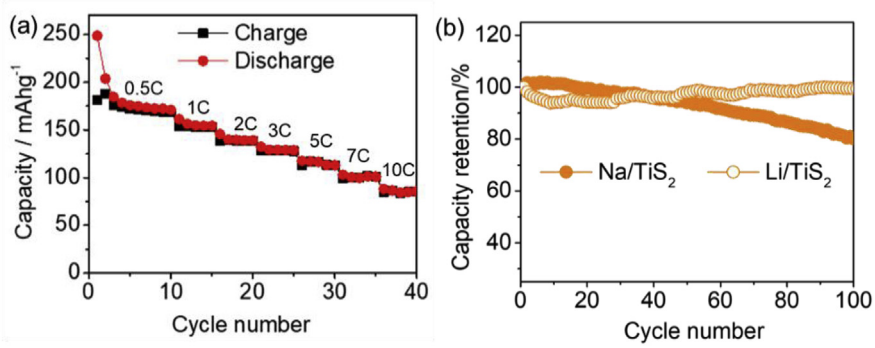

Fig. 4. (a) Rate capability of TiS_2 electrode, (b) Comparison of capacity retention between Na/TiS_2 and Li/TiS_2. The batteries were cycled at 0.5C.

further discharge, the position of the (001) peaks shifted to a slightly lower angle (Fig. 5b), suggesting a solid-solution type structural evolution with small shrinking of the lattice to 6.846 Å. Upon discharging to the second plateau, the peak intensity of phase 3 decreased, while a new peak appeared (phase 4). Again, the layer spacing along the *c* direction further reduced with increasing Na concentration in Na_xTiS_2. Nevertheless, the overall expansion of the layer space along the (001) plane was 15.2%, as it went from 5.698 Å for bulk TiS_2 to 6.564 Å for the fully sodiated Na_xTiS_2. This value is 8.8% larger than that of Li_xTiS_2 along the *c* axis and larger than most layered oxides used as Li-ion battery cathode material, such as the ~1.5% volume expansion for $LiCoO_2$ [7].

During the de-sodiation process, although the main peak transformed back to its original position at the fully de-sodiated state, a weak diffraction peak at 12.4° was observed (Fig. 5b), which is associated with the existence of phase 3. This indicates that not all the Na^+ can be de-inserted from TiS_2 and transformation between phase 3 and phase 2 is partially irreversible. This irreversibility was also observed in TiS_2 electrodes for Mg^{2+} intercalation/de-intercalation [20]. This irreversible phase remained within the core of the particles due to the micrometer-sized TiS_2 particles that would have an extra-large ionic diffusion length. Meanwhile, it is noted that phase 3 transformed

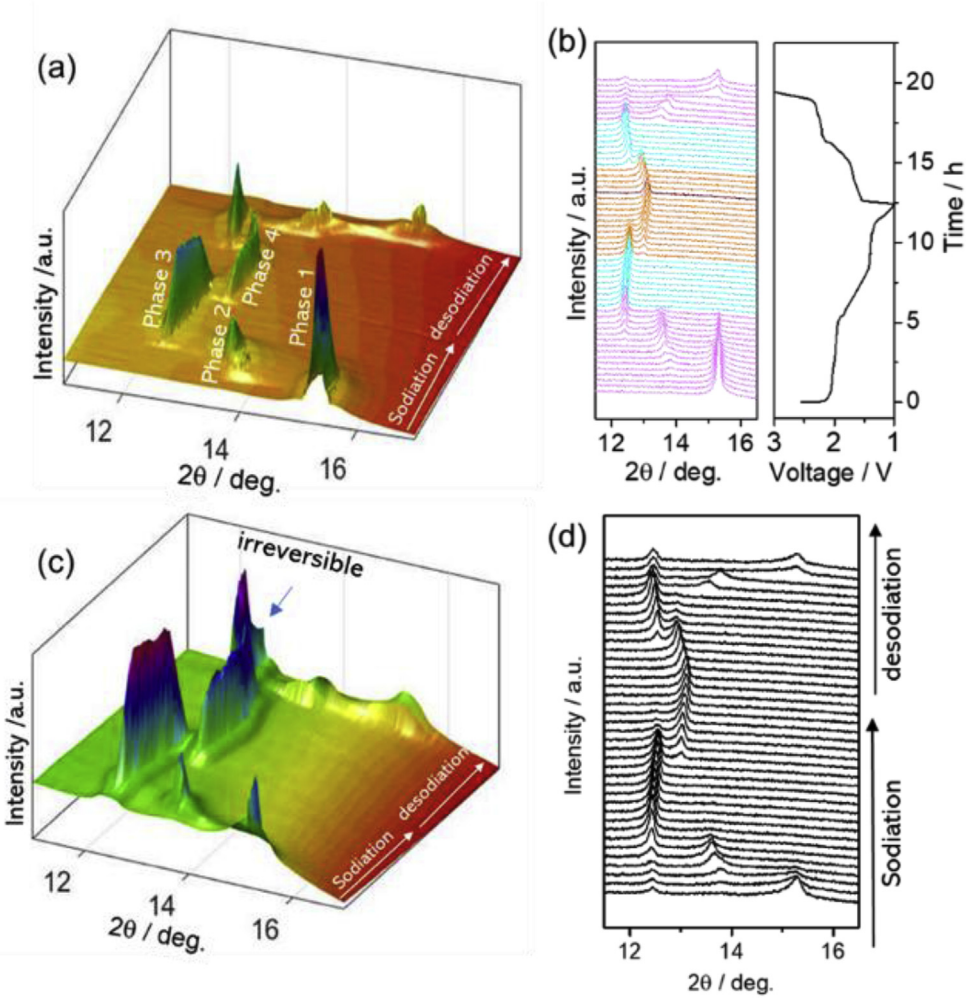

Fig. 5. In-situ XRD results of the TiS_2 electrode for the 1st cycle: (a) 3D plot and (b) line patterns and the corresponding charge–discharge profile of the electrode. In-situ XRD results of the TiS_2 electrode for the 2nd cycle: (c) 3D plot and (d) line patterns.

completely to phase 4 during the 2nd discharge (Fig. 5c and d), but it still didn't fully convert to phase 2 during the charge process. This observation demonstrates that phase 3 is highly active to Na^+ intercalation but is less active to Na^+ de-intercalation. Moreover, the peak intensity of phase 3 after the second cycle is stronger than that after the first cycle (Fig. 5c), which means that the irreversible phase accumulated in the electrode material with each cycle and this lead to capacity decay during long-term cycling. After 100 cycles, ex-situ XRD patterns (Fig. S6) showed that (001) diffraction peaks for bulk/pristine TiS_2 disappeared entirely. The accumulation of the irreversible phase 3 could be confirmed by the EDS results of STEM in Fig. S7, and it is seen that all three elements, Na, Ti and S were distributed homogeneously in the electrode at the de-sodiated state after 3 and 100 cycles. Particularly, the percentage of Na in the electrode was 5.01% after 3 cycles and had increased to 9.41% after 100 cycles (Table S1). Compared to the Na/TiS_2 system, no obvious changes were observed in the XRD pattern of the TiS_2 electrode in Li/TiS_2 battery (Fig. S8) before and after 100 cycles. This strongly suggests better stability of TiS_2 in Li/TiS_2 during Li^+ intercalation/de-intercalation.

It is expected that the irreversible phase transformation and volume expansion induced stress and strain that may cause crack formation and mechanical degradation, further contributing to the severe capacity decay [33,34]. To investigate the mechanical degradation of TiS_2, spherical aberration corrected TEM and geometric phase analysis were carried out. Fig. 6 compares the TEM images and the corresponding strain map obtained by the GPA method for the TiS_2 electrode before and after cycling. The strain mapping displays a homogenous pattern in the whole region for the fresh electrode (Fig. 6a), whose strain components are close to zero. While an abrupt strain field in ε_{xx}, ε_{yy}, ε_{xy} is seen clearly after 10 cycles (Fig. 6b), indicating the severe lattice distortion for the electrode after the sodiation/de-sodiation process. On the contrary, the lattice strain of the TiS_2 electrode cycled against Li is significantly less as seen in Fig. 6c.

SEM was carried out to identify the microstructural changes of the TiS_2 cathodes upon cycling. As shown in Fig. S9, no obvious fracture was observed during the first 10 cycles, while small cracks appeared on the surface of the particles after 20 cycles. The extent of damage is illustrated by the STEM images in Fig. 7, which revealed that intragranular cracks formed in the TiS_2 after 100 (Fig. 7a) and 500 cycles (Fig. 7b) in SIBs. Significantly more cracks are visible after 500 cycles. EDS mapping was also performed to observe the distribution of Ti, S, and Na after 100 and 500 cycles. It is seen that Na was present even though these images were taken after complete de-sodiation, which is consistent with the in situ XRD results of Fig. 5 that depicted the formation of irreversible Na-based compounds. The STEM images (Fig. S10) for the lithiated TiS_2 particles did not reveal such damage, but instead indicated very good mechanical stability in Li/TiS_2 after 100 cycles.

3.4. Mechanics model of lithiation- and sodiation-induced stresses

The cracks observed in Fig. 7 resulted from the high stresses that developed during the ion-insertion in the charge and discharge process. Modelling, hence, the stress evolution during cycling is crucial in understanding the mechanical influence on the electrochemical performance of electrode materials. A three-dimensional spherical model is established to illustrate the different lithiation- and sodiation-induced stresses that a TiS_2 particle experiences. Due to spherical symmetry, the shear stress components are neglected and the two tangential normal stress components are identical, i.e, $\sigma_\theta = \sigma_\phi$. Each point on the particle has three nonzero stress components, the hoop (tangential) stresses ($\sigma_\theta = \sigma_\phi$) and the radial stress (σ_r) which are along the tangential and radial directions, respectively. By treating the ion-insertion similarly to thermal expansion [35–36], the constitutive relations for the stresses (σ_r and σ_θ) can be written for ion diffusion as:

$$\left.\begin{aligned}\sigma_r &= \frac{E}{(1+\upsilon)(1-2\upsilon)}\left[(1-\upsilon)\frac{du}{dr} + 2\upsilon\frac{u}{r} - (1+\upsilon)\beta c\right]\\ \sigma_\theta &= \frac{E}{(1+\upsilon)(1-2\upsilon)}\left[\frac{u}{r} + \upsilon\frac{du}{dr} - (1+\upsilon)\beta c\right]\end{aligned}\right\} \quad (1)$$

where E is the Young's modulus, υ is Poisson's ratio, u is the radial displacement, β is the expansion coefficient of the spherical particle, and c is the concentration during ion insertion.

The stress field can therefore be obtained during charging. Fig. 8a–b shows the schematics of the diffusion-induced stress in a spherical free standing particle during the sodiation (Fig. 8a)/lithiation (Fig. 8b) process. For the sodiation/de-sodiation process, the volume changes are high (17.7%), hence a volume mismatch occurs between the sodiated TiS_2 shell and pristine core. A sharp reaction front separates the sodiated phase and unreacted phase (Fig. 8a), indicating that sodiation occurs in a two-phase process. The volume expansion of TiS_2 upon lithiation is relatively small (8.8%) allowing for a gradual change in Li concentration and undergoing a solid solution reaction, shown in Fig. 8b. The differences in lithiation versus sodiation are modelled by using a different concentration profile for each case. Since lithiation occurs via a solid solution reaction, an extended concentration profile of lithium along the radial direction is assumed, while to capture sodiation a steeper step-like concentration profile is generated, which can account for the sharp phase-boundary and two phase sodiation [37]. (Details are included in supplementary materials.) Fig. 8c presents the normalized concentration profile with respect to the normalized radial distance (dashed lines for the lithiation and solid lines for sodiation) [37]. The concentration is normalized by its maximum value at the fully lithiated/sodiated state and the radial distance (r) is normalized by the radius (R) of the TiS_2 particle.

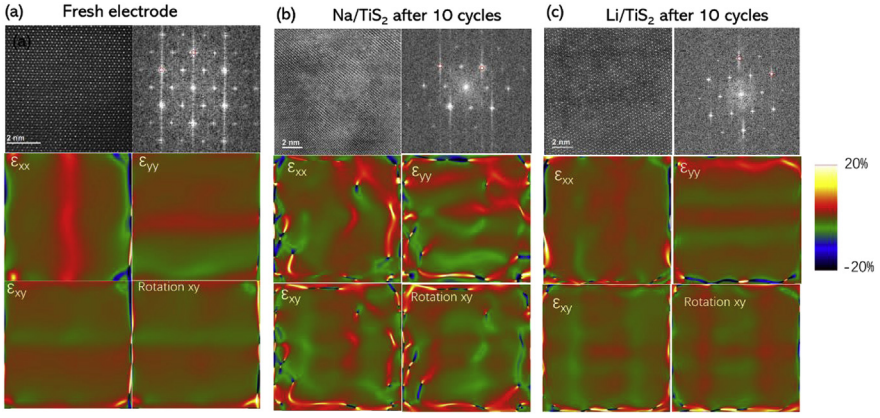

Fig. 6. HR-TEM images and the corresponding strain map using GPA method. (a) Fresh TiS_2 electrode. TiS_2 electrode after 10 cycles for (b) Na battery and (c) Li battery.

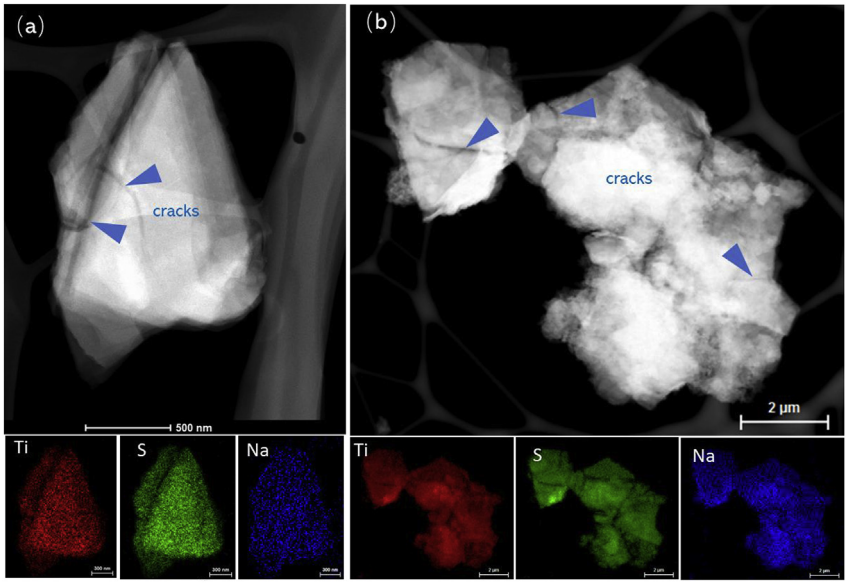

Fig. 7. STEM images and the corresponding element map for TiS_2 electrode after (a) 100 cycles and (b) 500 cycles.

Fig. 8d–f displays the stress evolution during the first lithiation and sodiation. It is seen that $\sigma_r \approx \sigma_\theta$ and they both remain constant in the pristine TiS_2 regions for sodiation. During sodiation $\sigma_r \approx \sigma_\theta$ are 2.13 GPa, 3.22 GPa and 3.63 GPa when 50% of the sodiated region extends up to 0.25*R*, 0.5*R* and 0.75*R*, respectively, *R* being the particle radius. The lithiation process, occurs via a solid reaction, therefore, there is no abrupt change in the concentration profile, as seen by the dashed lines in Fig. 8. When 50% of the lithiated region is located at the same positions (0.25*R*, 0.5*R* and 0.75*R*), the values of $\sigma_r \approx \sigma_\theta$ gradually decrease from the center to the surface of the particle. Overall it can be seen that for the lithiated and sodiated regions, σ_r gradually decreases to zero from the phase-boundary interface to the outer surface, and σ_θ transits from tensile (positive value), in lithium-poor and sodium-poor regions, to compressive (negative value), in lithium-rich and sodium-rich regions. The effective von Mises stress (σ_e) is the main factor contributing to failure and fracture and is defined as

$$\sigma_e = |\sigma_r - \sigma_\theta| \quad (2)$$

For the unreacted regions during sodiation, σ_e remains zero, while for the sodiated regions σ_e increases rapidly to a maximum value and then gradually decreases. The maximum value of σ_e occurs in sodiated regions that are very close to the phase-boundary (sodiated vs. unsodiated) interface. The maximum values of σ_e during sodiation are 3.72 GPa, 4.38 GPa and 4.65 GPa, which correspond to the concentration profiles of (I), (II) and (III) in Fig. 8c, respectively. In contrast, σ_e shows a small variation over the entire region during the lithiation process, with the maximum values of σ_e being significantly lower than those for sodiation: 0.67 GPa, 1.07 GPa and 1.37 GPa for the concentration profiles of (I), (II) and (III) in Fig. 8c respectively. The significantly higher von misses stress values during sodiation, indicate that TiS_2 is more susceptible to failure/fracture during Na-ion insertion rather than lithiation, which is consistent with the cracks observed in SIBs in Fig. 7.

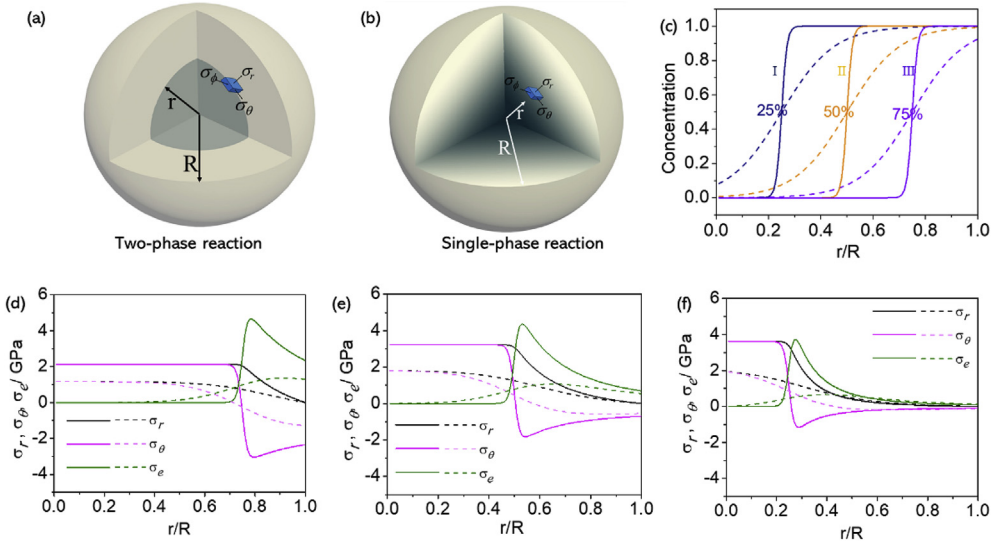

Fig. 8. Schematics showing the tangential stress components σ_θ, σ_ϕ and radial stress σ_r in: (a) Na-ion insertion in a TiS_2 spherical particle of radius *R*. A moving two-phase boundary exists between the pristine "core" of radius *r* and the "sodiated shell". (b) Li-ion insertion in a TiS_2 spherical particle of radius *R* without a sharp phase boundary. The abrupt color change in (a) represents a sharp phase boundary (reaction front) while the color gradient in (b) represents gradual change in lithium concentration with the highest concentration being at the surface of the particle. (c) Radial distributions of the normalized lithium or sodium concentration when 50% of the lithiated or sodiated region is located at 0.25*R*, 0.50 *R* and 0.75 *R* from the center of the particle (from left to right) respectively. (d) Radial distribution of σ_r. (e) Radial distribution σ_θ. (f) Radial distribution of the von Mises effective stress σ_e. The profiles in (d), (e), and (f) correspond to the Li or Na concentration profiles of (III), (II) and (I) in (c). (dashed lines: lithiation, solid lines: sodiation).

4. Conclusions

This article focused on examining the electrochemical and mechanical stability of TiS_2 cathodes in Na-ion cells. It was shown that the cycling stability was significantly affected by the electrolyte since it controls the side reactions that occur at the electrode-electrolyte interface with $NaFP_6$. EC/DMC electrolytes allowed for the highest capacity retention to be obtained: 203 mAh g^{-1} at 0.2 C and 88 mAh g^{-1} at 10 C, at a 92% retention over 50 cycles. Long term cycling revealed that TiS_2 was more stable during lithiation than sodiation. In-situ XRD illustrated that the electrochemical instability of the Na/TiS_2 system could be attributed to the formation of irreversible Na-containing phases and large volume changes (17.7% along the *c* direction). STEM images indicated that such structural changes resulted in severe mechanical strains and intragranular cracks in the TiS_2 particles during cycling with Na^+. The experimental observations were interpreted with continuum mechanics modelling which showed that the maximum effective von Mises stress at the interface between the ion-intercalated TiS_2 and pristine TiS_2 is about four times higher during sodiation than lithiation, making the electrode more susceptible to failure/fracture during sodiation.

Acknowledgements

The authors are grateful to the National Science Foundation for supporting this work through the CMMI grant CMMI-1762602. TEM work was performed at National High Magnetic Field Laboratory, which is supported by National Science Foundation Cooperative Agreement No. DMR-1644779 and the State of Florida.

Appendix A. Supplementary data

Supplementary data to this article can be found online at https://doi.org/10.1016/j.nanoen.2019.06.016.

References

[1] J.Y. Hwang, S.T. Myung, Y.K. Sun, Chem. Soc. Rev. 46 (2017) 3529–3614.
[2] S.W. Kim, D.H. Seo, X.H. Ma, G. Ceder, K. Kang, Adv. Energy Mater. 2 (2012) 710–721.
[3] H.L. Pan, Y.S. Hu, L.Q. Chen, Energy Environ. Sci. 6 (2013) 2338–2360.
[4] W. Hou, X. Guo, X. Shen, K. Amine, H. Yu, J. Lu, Nano Energy 52 (2018) 279–291.
[5] A. Konarov, J.H. Jo, J.U. Choi, Z. Bakenov, H. Yashiro, J. Kim, S.-T. Myung, Nano Energy 59 (2019) 197–206.
[6] N. Yabuuchi, M. Kajiyama, J. Iwatate, H. Nishikawa, S. Hitomi, R. Okuyama, R. Usui, Y. Yamada, S. Komaba, Nat. Mater. 11 (2012) 512.
[7] X. Lu, Y. Sun, Z. Jian, X. He, L. Gu, Y.-S. Hu, H. Li, Z. Wang, W. Chen, X. Duan, L. Chen, J. Maier, S. Tsukimoto, Y. Ikuhara, Nano Lett. 12 (2012) 6192–6197.
[8] D. Kim, E. Lee, M. Slater, W.Q. Lu, S. Rood, C.S. Johnson, Electrochem. Commun. 18 (2012) 66–69.
[9] H. Ye, C.-Y. Wang, T.-T. Zuo, P.-F. Wang, Y.-X. Yin, Z.-J. Zheng, P. Wang, J. Cheng, F.-F. Cao, Y.-G. Guo, Nano Energy 48 (2018) 369–376.
[10] J.H. Liu, H.Y. Chen, J.N. Xie, Z.Q. Sun, N.N. Wu, B.R. Wu, J. Power Sources 251 (2014) 208–214.
[11] J. He, C. Zhang, H. Du, S. Zhang, P. Hu, Z. Zhang, Y. Ma, C. Huang, G. Cui, Electrochim. Acta 178 (2015) 476–483.
[12] C. Shang, S. Dong, S. Zhang, P. Hu, C. Zhang, G. Cui, Electrochem. Commun. 50 (2015) 24–27.
[13] T. Wang, P. Hu, C. Zhang, H. Du, Z. Zhang, X. Wang, S. Chen, J. Xiong, G. Cui, ACS Appl. Mater. Interfaces 8 (2016) 7811–7817.
[14] E. Yang, H. Ji, Y. Jung, J. Phys. Chem. C 119 (2015) 26374–26380.
[15] D.S. Wang, Y.H. Liu, X. Meng, Y.J. Wei, Y.Y. Zhao, Q. Pang, G. Chen, J. Mater. Chem. A 5 (2017) 21370–21377.
[16] F. Xie, L. Zhang, Q. Gu, D. Chao, M. Jaroniec, S.-Z. Qiao, Nano Energy 60 (2019) 591–599.
[17] G.H. Newman, L.P. Klemann, J. Electrochem. Soc. 127 (1980) 2097–2099.
[18] D.S. Tchitchekova, A. Ponrouch, R. Verrelli, T. Broux, C. Frontera, A. Sorrentino, F. Barde, N. Biskup, M.E. Arroyo-de Dompablo, M.R. Palacin, Chem. Mater. 30 (2018) 847–856.
[19] J.E. Trevey, C.R. Stoldt, S.H. Lee, J. Electrochem. Soc. 158 (2011) A1282–A1289.
[20] X.Q. Sun, P. Bonnick, L.F. Nazar, ACS Energy Lett 1 (2016) 297–301.
[21] D. Tonti, C. Pettenkofer, W. Jaegermann, J. Phys. Chem. B 108 (2004) 16093–16099.
[22] J. Vinckeviciute, M.D. Radin, A. Van der Ven, Chem. Mater. 28 (2016) 8640–8650.
[23] Q. Li, Z. Yao, J. Wu, S. Mitra, S. Hao, T.S. Sahu, Y. Li, C. Wolverton, V.P. Dravid, Nano Energy 38 (2017) 342–349.
[24] I. Hasa, X.W. Dou, D. Buchholz, Y. Shao-Horn, J. Hassoun, S. Passerini, B. Scrosati, J. Power Sources 310 (2016) 26–31.
[25] H. Kim, J. Hong, Y.U. Park, J. Kim, I. Hwang, K. Kang, Adv. Funct. Mater. 25 (2015) 534–541.
[26] H. Kim, J. Hong, G. Yoon, H. Kim, K.Y. Park, M.S. Park, W.S. Yoon, K. Kang, Energy Environ. Sci. 8 (2015) 2963–2969.
[27] L.P. Wang, J. Zou, S.L. Chen, G. Zhou, J.M. Bai, P. Gao, Y.S. Wang, X.Q. Yu, J.Z. Li, Y.S. Hu, H. Li, Energy Storage Mater 12 (2018) 216–222.
[28] H.S. Ryu, J.S. Kim, J.S. Park, J.W. Park, K.W. Kim, J.H. Ahn, T.H. Nam, G.X. Wang, H.J. Ahn, J. Electrochem. Soc. 160 (2013) A338–A343.
[29] A. Chaturvedi, E. Edison, N. Arun, P. Hu, C. Kloc, V. Aravindan, S. Madhavi, Chemistryselect 3 (2018) 524–528.
[30] M.J. Hytch, E. Snoeck, R. Kilaas, Ultramicroscopy 74 (1998) 131–146.
[31] Z. Hu, Z.X. Tai, Q.N. Liu, S.W. Wang, H.L. Jin, S. Wang, W.H. Lai, M.Z. Chen, L. Li, L.N. Chen, Z.L. Tao, S.L. Chou, Adv. Energy Mater. 9 (2019).
[32] X.F. Bian, Y. Gao, Q.A. Fu, S. Indris, Y.M. Ju, Y. Meng, F. Du, N. Bramnik, H. Ehrenberg, Y.J. Wei, J. Mater. Chem. A 5 (2017) 600–608.
[33] Y.X. Zuo, J. Ma, N. Jiang, D.G. Xia, ACS Omega 3 (2018) 11136–11143.
[34] K. Wang, P. Yan, M. Sui, Nano Energy 54 (2018) 148–155.
[35] I. Tsagrakis, E.C. Aifantis, Gradient elasticity effects on the two-phase lithiation of LIB anodes, in: H. Altenbach, J. Pouget, M. Rousseau, B. Collet, T. Michelitsch (Eds.), Generalized Models and Non-classical Approaches in Complex Materials 2. Advanced Structured Materials, Springer, Cham, 2018, pp. 221–235.
[36] J. Réthoré, H. Zheng, H. Li, J. Li, K.E. Aifantis, J. Power Sources 400 (2018) 383–393.
[37] S. Huang, F. Fan, J. Li, S. Zhang, T. Zhu, Acta Mater. 61 (2013) 4354–4364.